Journal of Applied Polymer Science

Development of mesoporous titanium dioxide hybrid poly(vinylidene fluoride) ultrafiltration membranes with photocatalytic properties

Jianquan Zhao,[1,3] Chanjuan Liao,[2] Jing Liu,[3] Xinyu Shen,[3] Hua Tong[3]

[1]Analytical and Testing Center, Huazhong University of Science and Technology, Wuhan 430074, People's Republic of China
[2]College of Resources and Environment, Hunan Agricultural University, Changsha 410128, People's Republic of China
[3]College of Chemistry and Molecular Sciences, Wuhan University, Wuhan 430072, People's Republic of China
J. Zhao and C. Liao contributed equally to this article.
Correspondence to: H. Tong (E-mail: sem@whu.edu.cn)

ABSTRACT: A photocatalytic activity ultrafiltration membrane (UFM) was prepared by the blending of a poly(vinylidene fluoride) (PVDF) polymer with mesoporous titanium dioxide (M-TiO_2) particles via the phase-inversion method. The microstructure of the membrane and Ti element distribution were characterized by scanning electron microscopy and energy-dispersive X-ray spectroscopy. Their properties were also determined by thermogravimetric analysis, differential scanning calorimetry, Fourier transform infrared spectroscopy, tensile stress tests, contact angle tests, bovine serum albumin retention, water flux, and permeation flux. When the M-TiO_2 concentration reached 1 wt %, the thermal stability, mechanical properties, hydrophilicity, flux, and antifouling performance of the M-TiO_2/PVDF UFM were improved to an optimal value with the M-TiO_2 particles successfully entrapped and evenly distributed throughout the PVDF polymer matrix. Compared with the P25-modified PVDF UFM (1 wt %), the M-TiO_2-modified PVDF UFM (1 wt %) exhibited better photocatalytic activity and wonderful stability in the UV photocatalytic degradation of the organic dye Rhodamine B. © 2016 Wiley Periodicals, Inc. J. Appl. Polym. Sci. **2016**, *133*, 43427.

KEYWORDS: degradation; hydrophilic polymers; mechanical properties; membranes; morphology

Received 12 September 2015; accepted 9 January 2016
DOI: 10.1002/app.43427

INTRODUCTION

Because of the attractive thermal stability and chemical and mechanical resistances,[1–4] poly(vinylidene fluoride) (PVDF) membranes are widely used in filtration processes.[5–8] However, because of the hydrophobic nature of the PVDF material, PVDF membranes are prone to contamination by organic impurities during water and wastewater treatment; this leads to increased filtration resistance, a sharp decline in the membrane permeation flux,[9] and heavy membrane fouling.[10] Frequent cleaning increases the cost and causes secondary environmental pollution. Hence, hydrophilic modification is necessary to solve the membrane-fouling problem.

The use of titanium dioxide (TiO_2) materials in the hydrophilic modification of PVDF membranes has received considerable attention because of their high chemical stability, nontoxicity, and long-lasting hydrophilic effect.[11–18] Cao *et al.*[11] compared the performances of neat PVDF membrane and PVDF composite membranes with nanosized TiO_2 particles of different sizes and showed that the smaller TiO_2 nanoparticles could more remarkably improve the antifouling properties of the PVDF membranes. Yu *et al.*[12] reported that the TiO_2 particles improved the membrane strength and thermal stability of PVDF–TiO_2 composite ultrafiltration membranes (UFMs). In particular, the hydrophilicity and permeability increased dramatically as the amount of TiO_2 increased, whereas the retention properties of the UFM were nearly unchanged. Rahimpour *et al.*[13] prepared PVDF/sulfonated poly(ether sulfone) blend membranes modified with TiO_2 nanoparticles. The experimental results demonstrated that the antifouling properties of the membranes were improved through changes in the character of the membrane surface from hydrophobic to hydrophilic after the addition of TiO_2 in the casting solution. Yuliwati and Ismail[14] reported that PVDF/LiCl/TiO_2 membranes with loaded TiO_2 nanoparticles possessed enhanced membrane hydrophilicity. The maximum flux increased from 27.07 to 82.50 L m^{-2} h^{-1}, and the rejection of refinery wastewater was increased from 70.56 to 98.83%, respectively, at a 1.95 wt % TiO_2 concentration. Safarpour *et al.*[15,16] reported that the blended PVDF membrane containing a 0.05 wt % rGO/TiO_2 nanocomposite with a GO to TiO_2 ratio of 70:30 showed improved permeability and antifouling performance. Because of the high hydrophilicity of the rGO/TiO_2 nanocomposite, the rGO/TiO_2/PVDF

membranes were more hydrophilic and had higher pure water flux and flux recovery ratio values than the bare PVDF. Song *et al.*[17] reported that the addition of TiO_2 nanoparticles improved the hydrophilicity of the PVDF membrane and increased the rejection of the pepsin testing molecule. Wang *et al.*[18] broke the trade-off effect by the atomic layer deposition of TiO_2 onto PVDF membranes, with $TiCl_4$ and water as precursors. The deposition of TiO_2 enhanced the hydrophilicity and fouling resistance of the PVDF membranes; this was more evident at higher atomic layer deposition cycle numbers. These efforts demonstrate that the addition of nanosized TiO_2 fillers increases the membrane hydrophilicity and antifouling performance.

In fact, the technique of degrading organic substances on the membrane surface can also be used to reduce membrane fouling. Several researchers have demonstrated that anatase TiO_2 modified membranes exhibit an excellent photocatalytic activity that degrades many organic substances under UV irradiation.[15–21] Zhang *et al.*[21] successfully prepared TiO_2/Al_2O_3 composite membranes with photocatalytic capability from colloidal titanium sols via the sol–gel technique. The removal efficiency of the dye was markedly improved through a combination of photocatalysis and membrane techniques. The degradation of the dye helped enhance the composite membrane flux and prevent membrane fouling. Madaeni and Ghaemi[22] reported that membrane surfaces coated with TiO_2 particles not only conferred a photocatalytic property to the membrane but also increased its hydrophilicity. Djafer *et al.*[23] reported that titanium-based UFMs from commercial titanium hydrosol and alumina supports exerted high photocatalytic effects on methylene blue and phenol. Athanasekou and coworkers[24,25] developed composite TiO_2 photocatalytic γ–alumina ultrafiltration tubular membranes and nanofiltration membranes through the chemical-vapor layer-by-layer deposition of TiO_2, and the membranes were efficient in the photocatalytic degradation of methyl orange when they were evaluated in an innovative continuous flow reactor.

However, to the best of our knowledge, studies of the synthesis of mesoporous titanium dioxide (M-TiO_2) hybrid PVDF UFMs and the distribution of M-TiO_2 particles on the membrane surface and membrane cross surface of TiO_2-modified PVDF UFMs have rarely been conducted. Compared with conventional nanosized TiO_2 materials, M-TiO_2 has excellent hydrophilicity and exhibits a stable anatase phase and a distinctive highly ordered mesostructure; these contribute to its photocatalytic activity against organic pollutants. For one thing, an ordered mesoporous structure with a high specific surface area provides more photocatalytic reaction centers and active adsorption sites because a high specific surface area indicates a high adsorptive capacity and the active sites are usually located in the mesopores.[26] For another thing, the anatase phase of TiO_2 has been proven to have the highest photocatalytic activity compared with amorphous, rutile, and brookite TiO_2.[27,28] Thus, M-TiO_2 materials were used for PVDF UFM modification.

In this article, the synthesis of M-TiO_2 particles and the preparation of mesoporous titanium dioxide/poly(vinylidene fluoride) (P–MT) UFMs through the phase-inversion method are reported. The physical properties and filtration performance of the PVDF membranes was effectively improved with the addition of M-TiO_2 particles. The effects of the M-TiO_2 particles on the morphology, mechanical properties, thermal stability, membrane flux, hydrophilicity, and antifouling performance of the membranes were discussed. The photocatalytic activities of the P–MT membranes with different M-TiO_2 particle contents and a comparison with a P25/poly(vinylidene fluoride) where P25 is the degussa aeroxide TiO_2, (P–P) membrane with the P–MT (1 wt %) were evaluated through the photodecomposition of the rhodamine B (RhB) organic dye. The stability of P–MT before and after UV-irradiation application is also discussed.

EXPERIMENTAL

Materials

The triblock copolymer Pluronic P123 (weight-average molecular weight = 5800, EO20PO70EO20) was purchased from Aldrich. PVDF used was obtained from Shanghai New Materials Co., Ltd. (FR-904, intrinsic viscosity = 1.4–1.9 dL/g). P25 was obtained from Guangzhou Hualisen Trade Co., Ltd. (Guangzhou, China). Tetrabutyl titanate [$Ti(OC_4H_9)_4$], acetyl acetone [$CH_2(COCH_3)_2$], hydrochloric acid (HCl), ethanol (EtOH), RhB, polyvinylpyrrolidone (PVP; K30, weight-average molecular weight = 25,000–40,000), dimethylformamide, and dimethylacetamide (DMAC) were procured from Sinopharm Chemical Reagent Co., Ltd. Bovine serum albumin (BSA; weight-average molecular weight = 67,000) was provided by Shuangxuan Microorganism Substrate Plant in Beijing. All chemicals were analytical grade and were used as received without further purification. Ultrapure water (18.2 MΩ) was obtained from a Milli-Q water system.

Synthesis of Highly Ordered Mesoporous Anatase TiO_2 Particles

Highly ordered mesoporous anatase TiO_2 particles were synthesized by a sol–gel method in an acidic medium, with triblock copolymer P123 as a template. A typical procedure was as follows.[26] P123 was dissolved in an ethanolic HCl solution (with a small quantity of H_2O added) and stirred for 1 h. Then, $CH_2(COCH_3)_2$ was added to this solution under stirring for 20 min. $Ti(OC_4H_9)_4$ was added to the solution, and this mixture was further stirred in a sealed bottle at room temperature. The final molar ratio was $Ti(OC_4H_9)_4$/P123/EtOH/HCl/$CH_2(COCH_3)_2$/H_2O = 1:0.01:12.86:0.79:0.01:4.89. After the mixture was stirred for 24 h at a slow speed, the resulting sol solution was transferred into an open Petri dish and gelled at room temperature in air for 7 days. During the aging process, the relative humidity was 70–75%. After aging, the as-made bulk samples were treated at 90 °C for 24 h to consolidate the inorganic network; they were then calcined in air at 400 °C for 3 h to remove the template. Finally, the desired M-TiO_2 particles were obtained.

Membrane Preparation

The phase-inversion method was used to fabricate the P–MT composite UFMs. Polymer solutions were prepared by the addition of M-TiO_2 particles into a solvent containing PVDF, PVP, and DMAC under stirring at 60 °C until we obtained an

Table I. Compositions of the Casting Solutions

Membrane	PVDF (wt %)	DMAC (wt %)	M-TiO_2 (wt %)	PVP (wt %)	M-TiO_2 (wt %; by weight of PVDF)
P-MT-0	20	76	0	4	0
P-MT-1	20	75.9	0.1	4	0.5
P-MT-2	20	75.8	0.2	4	1
P-MT-3	20	75.4	0.6	4	3
P-MT-4	20	75	1	4	5

optimal particle dispersion. The casting dopes were then kept in a vacuum oven at 60 °C to remove air bubbles.

Different M-TiO_2 particle concentrations (0, 0.5, 1, 3, and 5 wt %, by weight of PVDF) of the polymer dopes were prepared. These were was denoted as P–MT-0, P–MT-1, P–MT-2, P–MT-3, and P–MT-4, respectively. The compositions of the polymer solutions are illustrated in Table I. The polymer solutions were cast uniformly onto a glass substrate via a self-made hand-casting knife and were then immersed in a deionized water bath after exposure to air. The flesh wet flat membranes were washed thoroughly with deionized water to remove residual solvent until they were used as samples for characterization. The thickness of the wet sample membranes was kept at 250 μm.[29]

P–P with 1 wt % P25 particles was also prepared according to the previous steps.

Membrane Characterization

Analysis Apparatus. The M-TiO_2 particles were observed with an X-ray diffractometer (X'Pert PRO MRD, PaNalytical, The Netherlands) and transmission electron microscopy (TEM; JEM-2100, JEOL, Japan). The N_2 adsorption–desorption isotherm was determined on a Micromeritics Tristar 3000 system at 77 K. The sample was degassed in a vacuum at 180 °C before the measurements. The surface area of M-TiO_2 was obtained by the Brunauer–Emmett–Teller method, and the pore size distribution was estimated from the nitrogen-desorption branch of the isotherm by the Barrett–Joyner–Halenda model. The scanning electron microscopy (SEM) morphologies and energy-dispersive X-ray spectroscopy (EDX) analysis of the P–MT UFM were observed with a Quanta 200 (FEI, The Netherlands). The membrane surface roughness parameters were investigated by a SPM-9500J3 contact-mode atomic force microscope (Shimadzu, Japan). The thermal stability was analyzed with an SETSYS Evolution 16 thermogravimetric analyzer (Setaram, France) under the condition of heating the samples from room temperature to 800 °C at a rate of 10 °C/min under nitrogen gas. Differential scanning calorimetry (DSC) of the P–MT was performed with a Diamond DSC instrument (PerkinElmer). Samples of 7 mg or less were heated from 30 to 250 °C at a heating rate of 5 °C/min under a nitrogen atmosphere. The mechanical stability of the wet membranes was measured with an AGS-J (Shimadzu, Japan) universal tensile testing machine under ambient conditions. Three samples were tested, and the average value was recorded. Measurements were carried out at room temperature with a rate of pull of 2 mm/min. The contact angle (θ) was measured with a DSA100 instrument (Kruss, Germany), each concentration of the P–MT was measured at five different points, and the average of these values was used. The Fourier transform infrared (FTIR) spectra of the membranes were measured with a Nicolet 5700 spectrometer (Thermo Electron Corp.).

Flux, BSA Retention, and Ratio of Permeate Flux Decline. The flux of the membranes was carried out with a 50-mL, stirred (500 rpm), dead-end filtration instrument with a membrane area of approximately 11.6 cm^2. The wet membrane was filtered with water for 40 min at 0.1 MPa to obtain a steady flux. After that the BSA retention was measured with a 200 mg/L BSA aqueous solution. The protein concentration in the solution and the permeation was tested through a UV-2550 spectrophotometer at the maximum wavelength (nm) (λ_{max}) of 280 nm.

The water flux (J_w) was determined with the following equation.

$$J_w = \frac{Q}{A \times \Delta T} \tag{1}$$

where Q is the volume of water permeated (L), A is the effective membrane area (m^2), and ΔT is the sampling time (h).

The BSA retention (R%) was calculated by eq. (2):

$$R\% = \frac{C_f - C_p}{C_f} \times 100\% \tag{2}$$

where C_f and C_p are the concentrations of BSA in the feed and the permeate, respectively.

The ratio of the permeate flux decline (m%) was calculated as follows:[29]

$$m\% = \frac{J_0 - J_1}{J_0} \times 100\% \tag{3}$$

where J_0 and J_1 are the initial permeate flux and the stable permeate flux of the BSA solution, respectively.

Membrane Porosity and Average Pore Size. The porosity was determined by the dry–wet weight method.[30] The porosity (ε; %) of the membrane was measured with eq. (4)[31]:

$$\varepsilon = \frac{(W_1 - W_2)/\rho_{water}}{(W_1 - W_2)/\rho_{water} + W_2/\rho_{PVDF}} \times 100\% \tag{4}$$

where W_1 is the weight of the wet membrane, W_2 is the weight of the dry membrane, ρ_{water} is the density of water at 25 °C (kg/m^3), and ρ_{PVDF} is the apparent density of the dry membrane (kg/m^3). Five samples were measured, and the average value was taken.

According to the Guerout–Elford–Ferry equation, the average pore size (r_m; m) could be determined by the filtration velocity method with the following equation[31]:

$$r_m = \sqrt{\frac{(2.9 - 1.75\varepsilon) \times 8\eta l Q_t}{\varepsilon A \times \Delta P}} \tag{5}$$

where η is the water viscosity at 25 °C, l is the membrane thickness (m), Q_t is the quantity of the permeate water per unit

time (m^3/h), and ΔP is the operational cross-membrane pressure drop.

Photocatalytic Activity Test

Photocatalytic activity tests of the P–MT and the P–P were performed by the photodegradation of the RhB solution under UV irradiation at room temperature in a darkroom. The UV source was a 250-W, high-pressure Hg lamp (maximum emission = 365 nm). The lamp was placed 30 cm above the RhB solution and was kept cool by a Silex glass recirculating water jacket (Pyrex).[26] In a typical protocol, all types of composite membranes were cut into a circular shape with a diameter of 45 mm and were immersed into the RhB dye solution (80 mL, $C_0 = 2 \times 10^{-5} M$, pH 6.0, where C_0 is the initial concentration of RhB dye solution) under stirring in the dark for 30 min, and then, the reaction mixture was exposed to the UV light with continuous magnetic stirring. The RhB solution (1 mL) was analyzed every 20 min with a UV–visible scanning spectrophotometer (UV-2550, Shimadzu, Japan) at $\lambda_{max} = 554$ nm.

RESULTS AND DISCUSSION

Microstructure of the M-TiO_2 Particles

Figure 1 shows the X-ray diffraction (XRD) pattern of the TiO_2 sample calcined at 400 °C for 3 h in air. Eight diffraction peaks appeared and were indexed as the (101), (004), (200), (211), (204), (220), (215), and (224) reflections of the anatase phase (JCPDS No. 21-1272). These peaks indicated the formation of TiO_2 nanocrystals after the calcination at 400 °C. The TEM image of the TiO_2 sample (Figure 2) clearly showed uniform, well-ordered hexagonal arrays in a large area and, thereby, confirmed the formation of highly ordered mesostructures. In addition, the pore size was estimated around 5.90 nm. The selected-area electron diffraction pattern of the TiO_2 sample (inset of Figure 2) showed a sequence of diffraction rings. This result was consistent with the polycrystalline anatase structure (JCPDS No. 21-1272) shown in the XRD pattern. This finding confirmed that the mesoporous walls consisted of crystalline TiO_2 anatase nanoparticles. The N_2 adsorption–desorption isotherm and the corresponding pore size distribution curve of the TiO_2 particles are shown in Figure 3. The isotherm (inset of Figure 3) could be classified as type IV; this was characteristic of mesoporous materials according to the IUPAC nomenclature.[32] The narrow pore size distribution curve (Figure 3) indicated a high degree of order on the mesoporous structures, and the estimated pore size was 5.93 nm; this was in accordance with the TEM analysis results. Meanwhile, the corresponding Brunauer–Emmett–Teller surface area and total pore volume were 122.42 m^2/g and 0.2779 cm^3/g, respectively. These results demonstrate that the obtained TiO_2 sample was in the crystalline anatase phase and had an ordered mesoporous structure with a high specific surface area, which was advantageous for the adsorption of water and hydroxyl groups.[33]

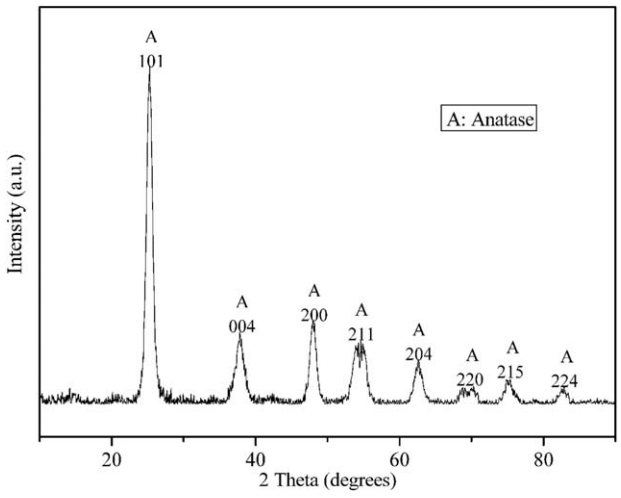

Figure 1. XRD pattern of the M-TiO_2 sample calcined at 400 °C for 3 h in air.

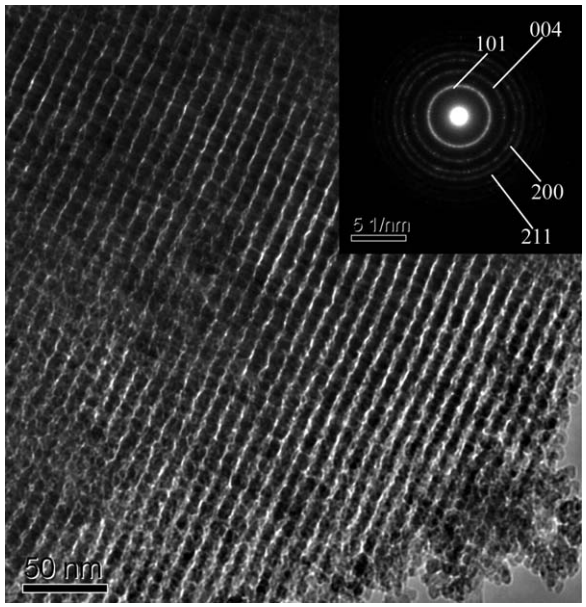

Figure 2. TEM image of the M-TiO_2 sample after calcination at 400 °C for 3 h. The inset shows the corresponding selected-area electron diffraction pattern.

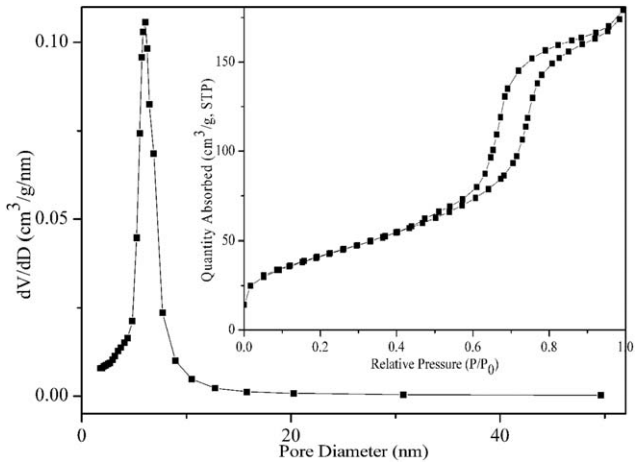

Figure 3. N_2 adsorption–desorption isotherm (inset) and Barrett–Joyner–Halenda pore size distribution curve of the M-TiO_2 particles prepared at 400 °C for 3 h. dV/dD, dVolume/dDiameter; STP, standard temperature and pressure; P/P_0, pressure for measuring point/the saturated vapor pressure of nitrogen in liquid nitrogen.

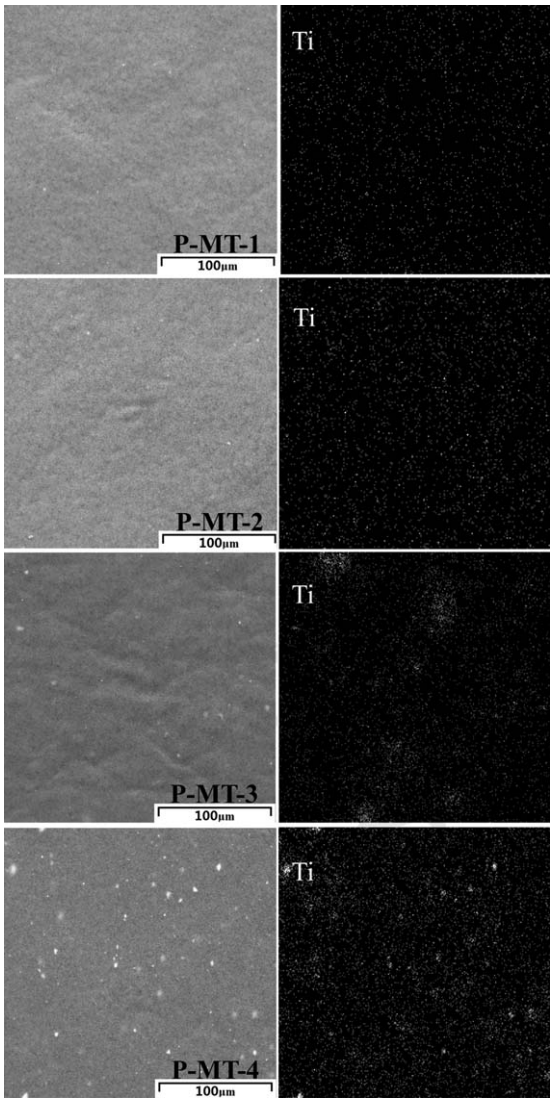

Figure 4. Surface morphology (SEM images, left side) and Ti distribution (EDX mapping, right side) of the P–MT composite membranes (P–MT-1, P–MT-2, P–MT-3, and P–MT-4).

Morphology Study

P–MT was prepared by the phase-inversion method. The top surface and cross-sectional SEM images of the P–MT are shown in Figures 4 and 5, respectively. The same membrane cross sections are exhibited (Figure 5) with similar relatively thick skin layers, inner fingerlike porous–surface structures, and sponge–wall porous structures. In addition, all of the membranes appeared to have typical asymmetric morphologies. The inner fingerlike pores linked by sponge walls consisted of large numbers of micropores for the fingerlike pores to communicate with each other.[29] As shown in Table II, with increasing concentration of M-TiO_2 in the modified membranes, the value of membrane porosity, average pore size, and BSA retention had a slight floating trend. These results confirmed that the addition of M-TiO_2 with a concentration below 5 wt % had no apparent influence on the integral membrane structure. The SEM images in Figures 4 and 5 also showed that the M-TiO_2 particles, which were detected by EDX analysis, were uniformly distributed on and nearby the membrane surface and in the membrane inner pore structure. However, we observed that more and larger particle aggregations took place with the increasing M-TiO_2 concentration from 3 to 5 wt %.

EDX analysis was carried out to investigate the distribution of M-TiO_2 particles on the top surfaces and cross sections of the membranes with different M-TiO_2 concentrations. The experimental values of the Ti content on the top surface of the P–MT are shown in Table III. With the addition of M-TiO_2 from 0.5 to 5 wt %, the experimental values of Ti on the top surface (0.17, 0.28, 0.76, and 1.40 wt %, respectively) increased gradually. The EDX images of titanium mapping corresponding to the SEM results are shown in Figures 4 and 5 (right side).

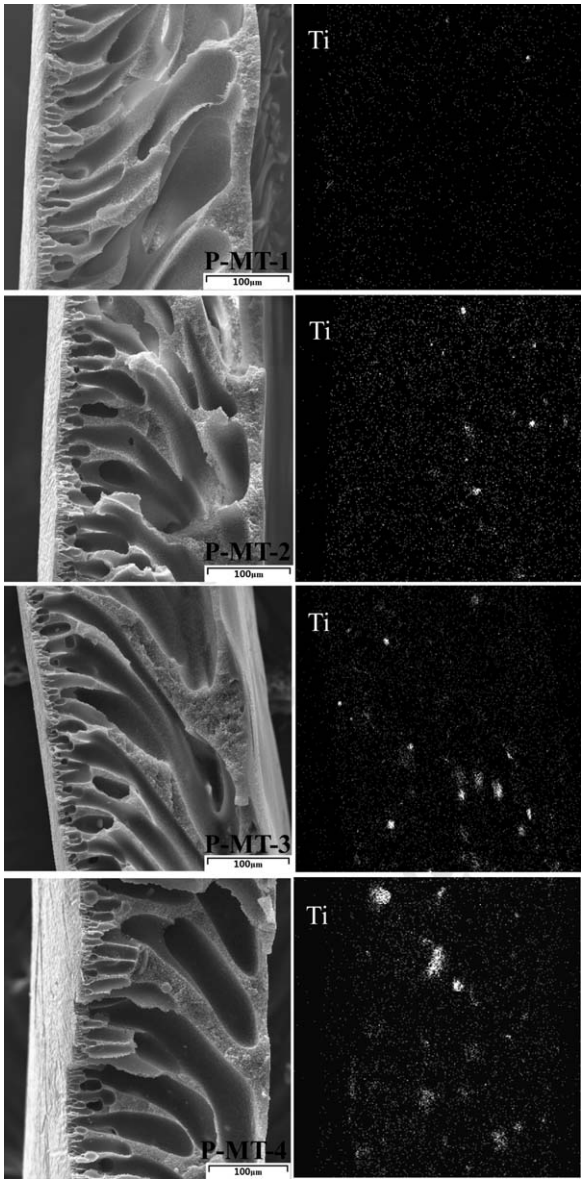

Figure 5. Cross-sectional morphology (SEM images, left side) and Ti distribution (EDX mapping, right side) of the P–MT composite membranes (P–MT-1, P–MT-2, P–MT-3, and P–MT-4).

Table II. Porosity Ratio, Average Pore Size, and BSA Retention of the P–MT UF Membranes

Membrane	Porosity (%)	Average pore size (10^{-8} m)	BSA retention (%)
P-MT-0	71.5 ± 0.3	8.5 ± 0.2	94.7
P-MT-1	68.7 ± 0.1	8.4 ± 0.1	95.1
P-MT-2	69.8 ± 0.2	8.3 ± 0.3	94.8
P-MT-3	68.8 ± 0.3	8.6 ± 0.2	94.5
P-MT-4	67.6 ± 0.4	8.9 ± 0.3	93.6

When the concentrations of added M-TiO_2 were 0.5 and 1 wt % (P–MT-1 and P–MT-2), the Ti elements were uniformly distributed throughout the top surface and pore walls in the cross section, and no Ti aggregation observed. This result could be explained by the penetration of the M-TiO_2 particles into the hybrid membrane and their subsequent uniform distribution. Meanwhile, as the M-TiO_2 concentration in the membrane increased, the growth of Ti scanning spots was also observed on P–MT-3 and P–MT-4. These results were consistent with the related elemental Ti content data on the top surface, as given in Table III. However, when the added amount of M-TiO_2 increased from 3 to 5 wt %, the distribution of Ti was heterogeneous, and an increasing number of large Ti spots were observed both on the top surface and in the cross section of the EDX mapping. These results could be explained by the aggregation of the M-TiO_2 particles and was consistent with the SEM results, as given in Figures 4 and 5 (left side).

The three-dimensional atomic force microscopy (AFM) surface results of P–MT-0, P–MT-1, P–MT-2, P–MT-3, and P–MT-4 are shown in Figure 6. The surface roughness parameters of these membranes over 4.0 × 4.0 μm^2 areas are presented in Table III. As the M-TiO_2 concentration in the casting solution increased, all of the roughness parameters [the arithmetic mean roughness (R_a), the 10-point mean roughness (R_z), the square average roughness (R_{ms}), and the average height (R_v)] of the composite membranes decreased to a valley at 1 wt % M-TiO_2 and then slightly increased. Thus, the surface roughness of the membranes was clearly affected by the addition of M-TiO_2 particles in the casting solution, and P–MT-2 (which had a 1 wt % M-TiO_2 content) possessed smoother surface and denser skin.

Thermal Stability

The thermogravimetric analysis (TGA) and DSC thermal analysis results of the P–MT are illustrated in Figure 7 and Table IV. The decomposition temperature (T_d; defined as the temperature at 3% weight loss) and weight residue at 700 °C of the membranes increased with increasing M-TiO_2 concentration. These results show that the M-TiO_2 particles were successfully incorporated in the membrane and illustrated the good compatibility of the M-TiO_2 particles in the PVDF polymer matrix. Furthermore, the residual mass after decomposition depended on the amount of the inorganic component. As the M-TiO_2 content increased, more heat was absorbed by the M-TiO_2 particles in the membranes during heating, and more interaction was increased between the PVDF chains and M-TiO_2 surface groups. Because of the good thermal transmission properties, the M-TiO_2 particles might have strongly hindered the volatility of the decomposed products obtained from pyrolysis and limited the continuous decomposition of the PVDF content.[12]

As shown in Figure 7, an endothermic melting peak of the PVDF polymer at 163 °C appeared in all of the DSC curves. With increasing concentration of M-TiO_2, the glass-transition temperature (T_g; in Table IV) of all of the modified membrane were significantly improved by more than 2 °C, and P–MT-2 had the best T_g (155.44 °C) of all. The addition of inorganic filler in PVDF could induce nucleation and increase the crystallinity of the polymer. The crystallinity of the composites affected the process of heat absorption and heat release and then affected the T_g of the system. However, as the filler content reached a certain amount, the aggregation of M-TiO_2 increased, and the nucleation effect decreased. This phenomenon eventually led to a T_g decrease. This result was consistent with the results of the morphology study.

Thus, with increasing addition of M-TiO_2 particles in the PVDF membranes, the decomposition of the PVDF composite was delayed, and the T_d and T_g values of the P–MT were enhanced. The composite PVDF membrane had the best composite thermal stability when the concentration of M-TiO_2 was 1 wt %.

Mechanical Stability

In a compression system, excellent mechanical properties are significant for the industrial membranes. Therefore, the tensile strength and breaking elongation data of the PVDF composite membranes were obtained. The results of the mechanical strength test of the membranes are shown in Figure 8. When the loading amount of M-TiO_2 particles increased from 0 to 5 wt %, the tensile strength of the membranes increased and reached a peak (6.1 N) at 1 wt % M-TiO_2 and then decreased with further increases in the M-TiO_2 concentration. This trend was consistent with the trend of porosity variation shown in Table II. Meanwhile, the breaking elongation kept a steady flat when the M-TiO_2 amount increased from 0 to 1 wt % and then decreased from 23.4 to 20.1% with the further increase in the M-TiO_2 concentration. These results could be interpreted by the uniform dispersion of the M-TiO_2 particles, the uniform porosity, and the dense pore structure in the hybrid membranes (0.5 and 1 wt %); this served as the physical crosslinkage that bore

Table III. Ti Contents and AFM Parameters on the Surface of the P–MT Composite Membranes

Membrane	Ti (K) element content (wt %)	Surface roughness (4 × 4 μm^2)			
		R_a (nm)	R_z (nm)	R_{ms} (nm)	R_v (nm)
P-MT-0	—	34.31	184.14	44.06	202.40
P-MT-1	0.17	27.05	119.11	34.23	112.14
P-MT-2	0.28	26.76	119.26	33.65	98.94
P-MT-3	0.76	27.39	121.16	34.59	110.66
P-MT-4	1.40	30.38	135.32	37.77	113.83

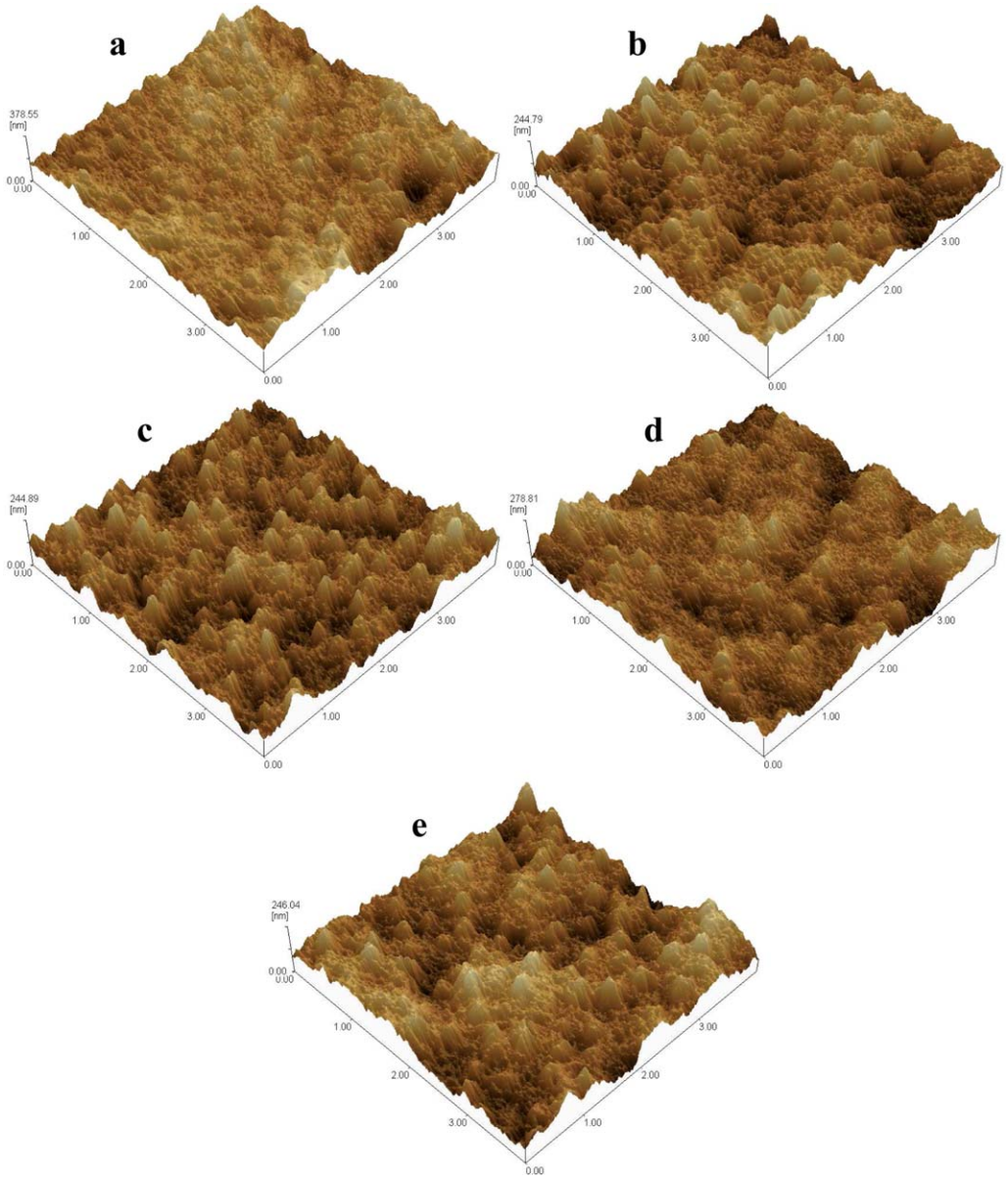

Figure 6. Three-dimensional AFM surface images of the P–MT composite membranes: (a) P–MT-0, (b) P–MT-1, (c) P–MT-2, (d) P–MT-3, and (e) P–MT-4. [Color figure can be viewed in the online issue, which is available at wileyonlinelibrary.com.]

the stress of the load and improved the mechanical strength of the membrane. However, excess M-TiO_2 (3 and 5 wt %) could cause the particle aggregation and reduce their uniform dispersion in the polymeric membrane; this led to the formation of defects, an increased average pore size (8.6×10^{-8} and 8.9×10^{-8} m), and stress convergence points in the membrane under the loading force and thus weakened the mechanical stability.[34] This explanation was supported by the SEM, EDX, and T_g results of the M-TiO_2 distribution, as shown in Figures 4 and 5 and Table IV.

Effect of the Addition of M-TiO_2 to the Membrane Flux and Antifouling Performance

The influences of the M-TiO_2 concentration on the membrane water flux were investigated through ultrafiltration experiments after compaction at 0.1 MPa for 40 min. As shown in Figure 9, the lowest water flux (368 L m^{-2} h^{-1}) was obtained for P–MT-0. Compared with that of P–MT-0, the water flux of the M-TiO_2 composite membranes increased, and all of the M-TiO_2 composite membranes showed a high constant BSA retention rate above 93% (Table II). This finding was attributed to the membrane hydrophilicity, which was measured through θ. The θ data of the P–MT are shown in Figure 9. Compared with that of neat PVDF membrane, the θ data of the modified membranes dramatically decreased; this indicated that the hydrophilicity of the membranes was effectively improved with the addition of the M-TiO_2 particles. The stable mesostructures of M-TiO_2 with high specific surface areas, which adsorbed water and hydroxyl groups, could have been responsible for the increase in the hydrophilicity.[35–37] With the further increase in

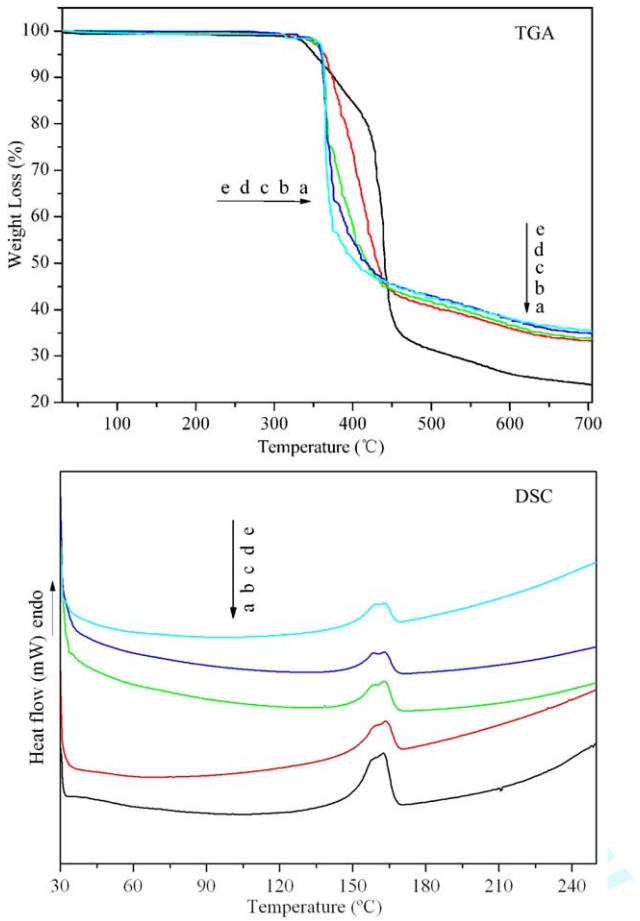

Figure 7. TGA and DSC curves of the P–MT composite membranes: (a) P–MT-0, (b) P–MT-1, (c) P–MT-2, (d) P–MT-3, and (e) P–MT-4. [Color figure can be viewed in the online issue, which is available at wileyonlinelibrary.com.]

$M\text{-}TiO_2$ (3 and 5 wt %), the decelerated decreasing trends of θ and the water flux were attributed to the presence of more $M\text{-}TiO_2$ particles and the increased occurrence of $M\text{-}TiO_2$ aggregation in the membrane matrix, respectively. The Ti content (Table III) and EDX images of each modified membrane discussed in the Morphology Study section also confirmed this trend.

The membrane hydrophilicity is a well-known major factor, which affects the surface-adsorption properties of the membranes.[38] The antifouling performance of the UFMs could be evaluated with the ratio of the permeate flux decline. Figure 10 shows the initial and stable permeate fluxes and the ratio of the permeate flux decline of P–MT during the filtration test of the

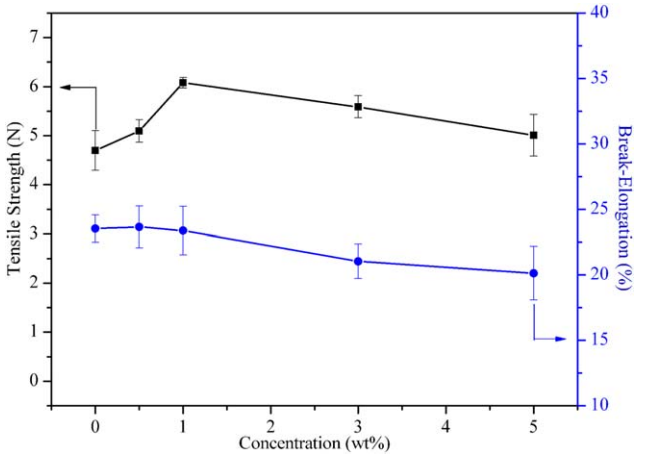

Figure 8. Tensile stress and strain at break of the P–MT composite membranes (0, 0.5, 1, 3, and 5 wt %). [Color figure can be viewed in the online issue, which is available at wileyonlinelibrary.com.]

BSA aqueous solution. As the amount of $M\text{-}TiO_2$ in the composite membranes increased, both the initial and stable permeate fluxes of the membranes effectively increased and reached a peak at 1 wt % $M\text{-}TiO_2$ and then slightly decreased as the $M\text{-}TiO_2$ concentration increased further. This trend was similar to the results of water flux (Figure 9). The ratio of permeate flux decline was calculated from the comparison of the initial permeate flux and the stable flux. As shown in Figure 10, the ratio of permeate flux decline gradually decreased as the amount of $M\text{-}TiO_2$ increased. It suggests that the antifouling performance of the P–MT was better than that of P–MT-0. This result could be attributed to the increased hydrophilicity and reduced surface roughness (discussed in the Morphology Study section) of the $M\text{-}TiO_2$ modified membranes.[39] Meanwhile, the $M\text{-}TiO_2$ composite membranes exhibited a more favorable antifouling performance combined with the degradation of organic substances on the membrane surface.

Photocatalytic Activities of the P–MT Membranes

The photocatalytic activities of P–MT were monitored through the photodegradation of an aqueous RhB solution under UV irradiation (Figure 11). As shown in Figure 11, we observed that the decrease phenomenon of RhB increased over time. After stirring in the dark for 30 min (the time that it took for the membranes to reach adsorption equilibrium in the RhB solution), similarly, a low RhB decrease (ca. 8%) occurred in all of the membranes; this could be attributed to the adsorption of the dye onto the membrane surface. It also showed that the P–MT-0 remained at adsorption equilibrium in the RhB solution after it was stirred in the dark for 150 min. These findings

Table IV. TGA and DSC Analysis Data for the P–MT Composite Membranes

Membrane	P-MT-0	P-MT-1	P-MT-2	P-MT-3	P-MT-4
Weight residue at 700 °C (%)	23.95	33.34	33.79	34.93	35.53
T_d (°C)	341.38	354.06	354.84	357.21	359.23
T_g (°C)	152.63	154.77	155.44	155.41	155.23

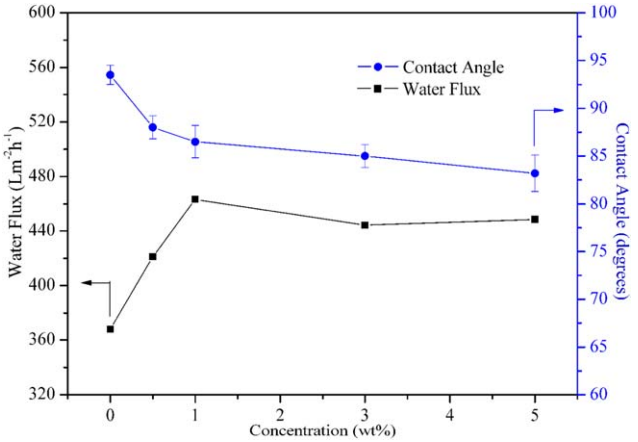

Figure 9. Water flux (0.1 MPa) and θs of the P–MT composite membranes (0, 0.5, 1, 3, and 5 wt %). [Color figure can be viewed in the online issue, which is available at wileyonlinelibrary.com.]

demonstrate that the addition of M-TiO_2 particles did not apparently affect the RhB adsorption of all of the membranes and membrane structures of the top surface and cross section for similar amounts of adsorbed RhB. After the UV-irradiation process for 120 min, the concentration of RhB occurring on P–MT-0 was reduced from 8 to 30%; this could be attributed to the self-degradation of RhB. During the UV-irradiation process, all of the P–MT clearly showed greater RhB degradation compared with the virgin membrane; these values were 55% (P–MT-1), 61% (P–MT-2), 62% (P–MT-3), and 65% (P–MT-4), respectively. This phenomenon was due to the photocatalytic degradation of the surface and near-surface M-TiO_2 particles in the composite membranes and part of the self-degradation of RhB. Compared with P–MT-0, P–MT showed better photocatalytic activities because of the photocatalytic activities of M-TiO_2 on the membrane surface and near the surface. Meanwhile, the photocatalytic activities gradually increased as the amount of M-TiO_2 particles in the PVDF membranes increased, with P–MT-4 exhibiting the best photocatalytic performance.

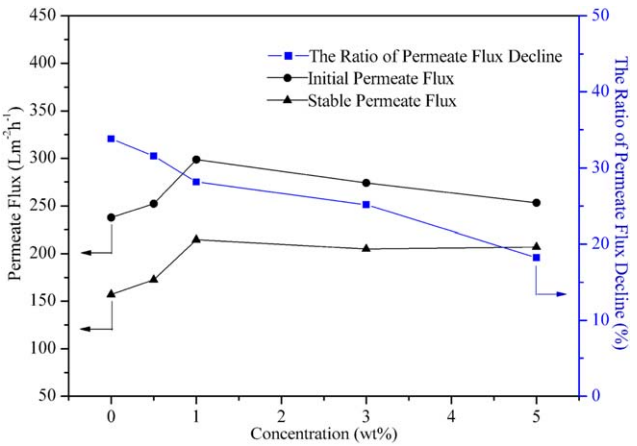

Figure 10. Permeate flux (BSA aqueous solution) and ratio of permeate flux decline of the P–MT composite membranes (0, 0.5, 1, 3, and 5 wt %). [Color figure can be viewed in the online issue, which is available at wileyonlinelibrary.com.]

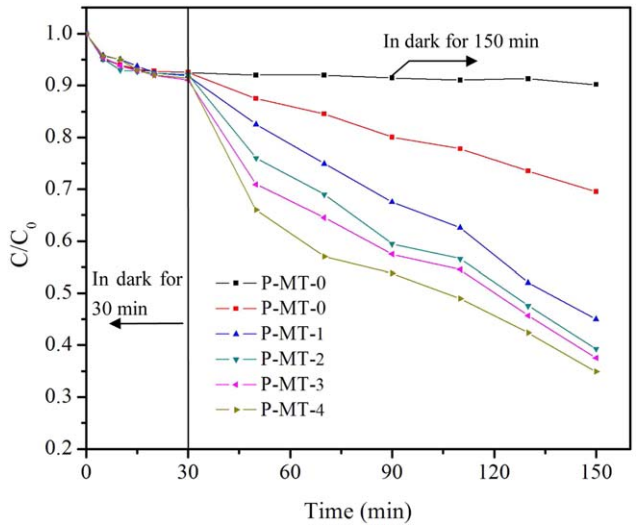

Figure 11. Photocatalytic properties of the P–MT composite membranes (RhB, $C_0 = 2.0 \times 10^{-5}M$, pH 6.0) under UV irradiation with increasing time. [Color figure can be viewed in the online issue, which is available at wileyonlinelibrary.com.]

For comparison, the photocatalytic activities of P–P (1 wt %) and P–MT (1 wt %) were also determined under identical conditions (Figure 12). As shown in Figure 12(a), under irradiation for 120 min, the RhB concentration decreased to 51.4 and 57.8% in the presence of P–P and P–MT, respectively. From the plots of $\ln(C_0/C)$ where C is the concentration of the RhB dye solution under UV photocatalytic application versus the irradiation time [Figure 12(b)], the corresponding UV photodegradation rate constants were 6.09×10^{-3} and 6.61×10^{-3} min^{-1} for the obtained P–P and P–MT, respectively. These results indicate that both P–P and P–MT exhibited a high photocatalytic activity. Furthermore, P–MT exhibited a better photocatalytic performance than P–P.

These results were attributed to the addition of the M-TiO_2 particles; this had a great effect on the photocatalytic activities of the PVDF membranes. As expected, first, the stable ordered mesostructures of the M-TiO_2 particles with a high specific surface area (122.42 m^2/g) offered plentiful active adsorption sites and photocatalytic reaction centers, many water molecules and hydroxyls were absorbed on M-TiO_2 (catalyst) and reacted with photoinduced holes, and more hydroxyl radicals (•OH) (strong oxidant) were generated within the mesopores.[26,40] Moreover, the diffusion distance of •OH formed inside the mesopores on M-TiO_2 was 1.3–2.4 nm; this was smaller than the pore diameter of M-TiO_2. This suggested that •OH formed inside the pore scarcely diffused out of the pores.[41] Therefore, the existence of such •OH formed inside the mesopores was beneficial for the enhancement of the photocatalytic activity. Then, the crystalline anatase phase showed a better photocatalytic activity than the pure amorphous, rutile, and brookite phases of TiO_2.[27,28] Furthermore, membrane pollution mainly occurred on the membrane surface layer during the ultrafiltration process, and the surface and near-surface M-TiO_2 embedded in the composite membranes effectively degraded the pollution on the membrane surface layer under UV irradiation. Therefore, the mesoporous anatase TiO_2 materials chosen

for PVDF membrane modification effectively enhanced the photocatalytic properties against the organic dye RhB.

To verify the stability of the PVDF membranes before and after UV-irradiation application, P–MT-0 and P–MT-2 were irradiated under UV for 2 h and marked as P–MT-0/UV and P–MT-2/UV, respectively. The FTIR spectra of P–MT-0, P–MT-0/UV, P–MT-2, P–MT-2/UV, and M-TiO_2 are shown in Figure 13; the M-TiO_2 had three characteristic peaks, broad bands below 1000 cm^{-1} assignable to the Ti—O—Ti crystal vibrations, and peaks at 1632 and 3447 cm^{-1} assignable to the blending vibrations of adsorbed water molecules and stretching vibrations from the hydroxyl groups, respectively. These peaks were not found in the P–MT-2 spectra with the small addition of M-TiO_2 in the PVDF matrix. The characteristic peaks of PVDF at 3700–3300, 1631, 1403, 1188, and 881 cm^{-1} were assigned to —OH stretching, H—O—H bending, C—H deformation, C—F stretching, and the amorphous phase of PVDF. In a comparison of P–MT-0 and P–MT-2 before and after UV irradiation, the IR characteristic peak of PVDF was found to have no visible change. It showed that UV irradiation did not affect the chemical-bond properties of PVDF, and P–MT-2 had wonderful chemical stability when used under UV photocatalytic application.

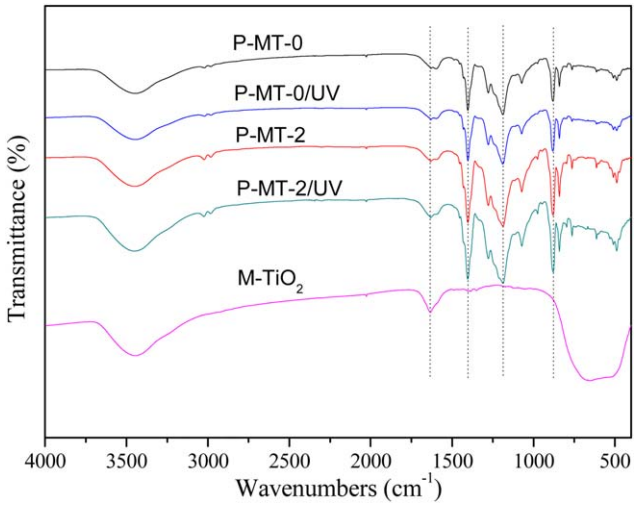

Figure 13. FTIR spectra of P–MT-0 (neat PVDF membrane), P–MT-0/UV, P–MT-2 (1 wt % M-TiO_2), P–MT-2/UV, and M-TiO_2. [Color figure can be viewed in the online issue, which is available at wileyonlinelibrary.com.]

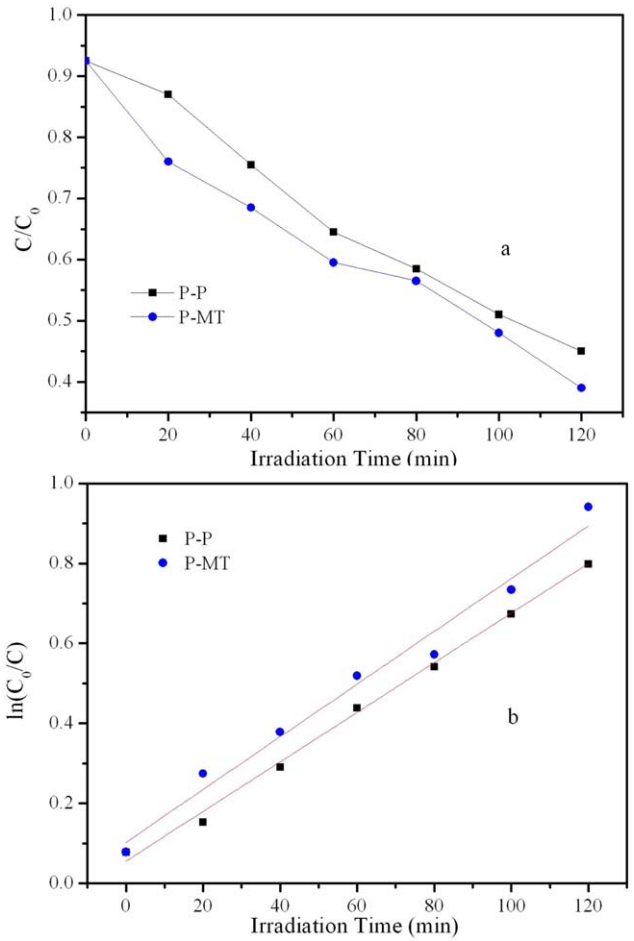

Figure 12. (a) Residual C/C_0 of an RhB dye solution ($C_0 = 2 \times 10^{-5} M$, pH 6.0) under UV photodegradation by P–P (PVDF UF membrane with 1 wt % P25 particles) and P–MT (PVDF UF membrane with 1 wt % M-TiO_2 particles) and (b) corresponding plots of $\ln(C_0/C)$ versus the irradiation time showing the fitting results from the pseudo-first-order reaction. [Color figure can be viewed in the online issue, which is available at wileyonlinelibrary.com.]

In this way, P–MT could be applied in the treatment of untreated wastewater from industrial or agricultural processes and containing organic pollutants, such as organic dyes, phenols, and pesticides.

CONCLUSIONS

P–MT composite UFMs with photocatalytic activity were synthesized with the phase-inversion method. The Ti elemental distribution, membrane morphology, membrane performance, and photocatalytic activity of the modified PVDF membranes with different M-TiO_2 contents were determined. As the amount of M-TiO_2 in composite membranes was increased, the thermal stability, hydrophilicity, antifouling performance, and photocatalytic activity of the composite membranes gradually improved. The M-TiO_2 particles showed no apparent effects on the integral membrane structure at a high constant BSA retention. When the M-TiO_2 concentration reached 1 wt %, the membrane surface roughness, mechanical properties, water flux, and permeate flux of the modified membranes reached an optimal value because of the uniform distribution of the M-TiO_2 particles on the membrane surface and inner pore structure and the interactions between the M-TiO_2 particles and the PVDF polymer. Moreover, P–MT has good chemical stability under UV photocatalytic applications, and P–MT exhibited better photocatalytic performance than the P–P membrane. Thus, the excellent characterization and uniform dispersion of the M-TiO_2 particles is important in the synthesis process of P–MT composite membranes, and this can effectively promote the performance of the modified membranes.

ACKNOWLEDGMENTS

Financial support for this work was provided by the National Natural Science Foundation of China (contract grant numbers 30900297 and 31071265), the Research Fund for the Doctoral Program of Higher Education (contract grant number 20090141120055), the Introduction of Talent Science Foundation of Hunan Agricultural University (contract grant number 620390112013), and the Yang Renbin Fund (contract grant number 011410500999).

REFERENCES

1. Nunes, S. P.; Peinemann, K. V. *J. Membr. Sci.* **1992**, *73*, 25.
2. Khayet, M.; Feng, C. Y.; Khulbe, K. C.; Matsuura, T. *Polymer* **2002**, *43*, 3879.
3. Wang, P.; Tan, K. L.; Kang, E. T.; Neoh, K. G. *J. Membr. Sci.* **2002**, *195*, 103.
4. Gryta, M.; Karakulski, K.; Morawski, A. W. *Water Res.* **2001**, *35*, 3665.
5. Zhang, M.; Zhang, A. Q.; Zhu, B. K.; Du, C. H.; Xu, Y. Y. *J. Membr. Sci.* **2008**, *319*, 169.
6. Wang, Z. W.; Wu, Z. C.; Hua, J.; Wang, X. H.; Du, X. Z.; Hua, H. *J. Hazard. Mater.* **2008**, *154*, 535.
7. Chen, Y. W.; Deng, Q. L.; Xiao, J. C.; Nie, H. R.; Wu, L. C.; Zhou, W. H.; Huang, B. W. *Polymer* **2007**, *48*, 7604.
8. Chang, C. L.; Chang, M. S. *J. Membr. Sci.* **2004**, *238*, 117.
9. Jian, K.; Pintauro, P. N.; Ponangi, R. *J. Membr. Sci.* **1996**, *117*, 117.
10. Teow, Y. H.; Latif, A. A.; Lim, J. K.; Ngang, H. P.; Susan, L. Y.; Ooi, B. S. *J. Appl. Surf. Sci.* **2015**, *132*, 41844.
11. Cao, X. C.; Ma, J.; Shi, X. H.; Ren, Z. *J. Appl. Surf. Sci.* **2006**, *253*, 2003.
12. Yu, L. Y.; Shen, H. M.; Xu, Z. L. *J. Appl. Polym. Sci.* **2009**, *113*, 1763.
13. Rahimpour, A.; Jahanshahi, M.; Rajaeian, B.; Rahimnejad, M. *Desalination* **2011**, *278*, 343.
14. Yuliwati, E.; Ismail, A. F. *Desalination* **2011**, *273*, 226.
15. Safarpour, M.; Khataee, A.; Vatanpour, V. *Sep. Purif. Technol.* **2015**, *140*, 32.
16. Safarpour, M.; Khataee, A.; Vatanpour, V. *Ind. Eng. Chem. Res.* **2014**, *53*, 13370.
17. Song, H. C.; Shao, J. H.; Wang, J. M.; Zhong, X. Q. *Desalination* **2014**, *344*, 412.
18. Wang, Q. Q.; Wang, X. T.; Wang, Z. H.; Huang, J.; Wang, Y. *J. Membr. Sci.* **2013**, *442*, 57.
19. Alaoui, O. T.; Nguyen, Q. T.; Mbareck, C.; Rhlalou, T. *Appl. Catal. A* **2009**, *358*, 13.
20. Liu, L. F.; Zheng, G. H.; Yang, F. L. *Chem. Eng. J.* **2010**, *156*, 553.
21. Zhang, H. M.; Quan, X.; Chen, S.; Zhao, H. M.; Zhao, Y. Z. *Sep. Purif. Technol.* **2006**, *50*, 147.
22. Madaeni, S. S.; Ghaemi, N. *J. Membr. Sci.* **2007**, *303*, 221.
23. Djafer, L.; Ayral, A.; Ouagued, A. *Sep. Purif. Technol.* **2010**, *75*, 198.
24. Athanasekou, C. P.; Romanos, G. E.; Katsaros, F. K.; Kordatos, K.; Likodimos, V.; Falaras, P. *J. Membr. Sci.* **2012**, *392*, 192.
25. Romanos, G. E.; Athanasekou, C. P.; Katsaros, F. K.; Kanellopoulos, N. K.; Dionysiou, D. D.; Likodimos, V.; Falaras, P. *J. Hazard. Mater.* **2012**, *211*, 304.
26. Zhao, J. Q.; Wan, P.; Xiang, J.; Tong, T.; Dong, L.; Gao, Z. N.; Shen, X. Y.; Tong, H. *Micropor. Mesopor. Mater.* **2011**, *138*, 200.
27. Schindler, K. M.; Kunst, M. *J. Phys. Chem.* **1990**, *94*, 8222.
28. Hsien, Y. H.; Chang, C. F.; Chen, Y. H.; Cheng, S. F. *Appl. Catal. B* **2001**, *31*, 241.
29. Liao, C. J.; Zhao, J. Q.; Yu, P.; Tong, H.; Luo, Y. B. *Desalination* **2010**, *260*, 147.
30. Chen, Z. A.; Deng, M. C.; Chen, Y.; He, G. H.; Wu, M.; Wang, J. D. *J. Membr. Sci.* **2004**, *235*, 73.
31. Yu, L. Y.; Xu, Z. L.; Shen, H. M.; Yang, H. *J. Membr. Sci.* **2009**, *337*, 257.
32. Sing, K. S. W.; Everett, D. H.; Haul, R. A. W.; Moscou, L.; Pierotti, R. A.; Rouquérol, J.; Siemieniewska, T. *Pure Appl. Chem.* **1985**, *57*, 603.
33. Peng, T. Y.; Zhao, D.; Dai, K.; Shi, W.; Hirao, K. *J. Phys. Chem. B* **2005**, *109*, 4947.
34. Wu, G. P.; Gan, S. Y.; Cui, L. Z.; Xu, Y. Y. *Appl. Surf. Sci.* **2008**, *254*, 7080.
35. Bae, T. H.; Kim, I. C.; Tak, T. M. *J. Membr. Sci.* **2006**, *275*, 1.
36. Kim, S. H.; Kwak, S. Y.; Sohn, B. H.; Park, T. H. *J. Membr. Sci.* **2003**, *211*, 157.
37. Madaeni, S. S.; Ghaemi, N.; Alizadeh, A.; Joshaghani, M. *Appl. Surf. Sci.* **2011**, *257*, 6175.
38. Yan, L.; Li, Y. S.; Xiang, C. B.; Xianda, S. *J. Membr. Sci.* **2006**, *276*, 162.
39. Liao, C. J.; Zhao, J. Q.; Yu, P.; Tong, H.; Luo, Y. B. *Desalination* **2012**, *285*, 117.
40. Wang, X. C.; Yu, J. C.; Ho, C. M.; Hou, Y. D.; Fu, X. Z. *Langmuir* **2005**, *21*, 2552.
41. Shiraishi, Y.; Saito, N.; Hirai, T. *J. Am. Chem. Soc.* **2005**, *127*, 12820.